

# Programmable terahertz metamaterials with non-volatile memory

**Benwen Chen**

Nanjing University

**Jingbo Wu**

Research Institute of Superconductor Electronics (RISE), School of Electronics Science and Engineering, Nanjing University <https://orcid.org/0000-0003-2969-5670>

**Weili Li**

Nanjing University

**Caihong Zhang**

Nanjing University

**Qiang Xue**

University of Electronic Science and Technology of China

**Yaojia Chi**

University of Electronic Science and Technology of China

**Qiye Wen**

University of Electronic Science and Technology of China

**Biaobing Jin** (✉ [bbjn@nju.edu.cn](mailto:bbjn@nju.edu.cn))

Nanjing University

**Jian Chen**

Research Institute of Superconductor Electronics (RISE), School of Electronics Science and Engineering, Nanjing University

**P. H. Wu**

Nanjing University

---

## Article

**Keywords:** Spatial light modulators (SLMs), terahertz metamaterials, electromagnetic information processing

**Posted Date:** March 25th, 2021

**DOI:** <https://doi.org/10.21203/rs.3.rs-287128/v1>

**License:**   This work is licensed under a Creative Commons Attribution 4.0 International License.

[Read Full License](#)

---

**Version of Record:** A version of this preprint was published at Laser & Photonics Reviews on January 25th, 2022. See the published version at <https://doi.org/10.1002/lpor.202100472>.

# Abstract

Spatial light modulators (SLMs) exhibited the powerful capability of controlling the electromagnetic wave. They have found numerous applications at terahertz (THz) frequencies, including wireless communication, digital holography, and compressive imaging. However, the development towards large-scale, multi-level and multi-functional THz SLM encounters technical challenges. Here, we present an electrically programmable THz metamaterial consisting of an array of  $8 \times 8$  pixels, in which the phase change material of vanadium dioxide ( $\text{VO}_2$ ) is embedded. After successfully suppressing the crosstalk from adjacent pixels, the THz wave could be modulated in a programmable manner. The switching speed of each pixel was on the order of 1 kHz. In particular, utilising the hysteresis effect of  $\text{VO}_2$ , the memory effect is demonstrated. The THz amplitude of each pixel can be written and erased by individual current pulses. Furthermore, multi-state THz images could be generated and stored, with a retention time of more than 5 hours. This programmable metamaterial with memory effect can be extended to other frequency bands and opens a route for electromagnetic information processing.

## Introduction

Spatial light modulator (SLM) has demonstrated the capability of manipulating the amplitude, phase, or polarisation state of electromagnetic wave. At terahertz (THz) frequencies, SLM has been used to address the technical challenges of THz applications, including beamforming<sup>1</sup>, compressive imaging<sup>2</sup>, and digital holography<sup>3</sup>. However, the bottleneck for THz SLM development is the lack of suitable natural materials and electronic components. In recent years, metamaterials offer us a powerful tool to manipulate electromagnetic waves in desirable ways<sup>4-6</sup>. The advances of digital and programmable metamaterials contribute to the rapid development of THz SLM<sup>7,8</sup>. A variety of metamaterial-based THz SLM has been demonstrated and used for information procession. The reconfigurability of THz wave modulation in these designs relied on tuneable materials such as semiconductors<sup>9,10</sup>, liquid crystals<sup>11</sup>, graphene<sup>12</sup> and phase-change materials<sup>13</sup> or micro-mirror arrays<sup>14-16</sup> and microfluidics<sup>17</sup>.

Towards practical applications, new challenges have emerged. The large-scale integrated multi-level SLMs are highly demanding to realize highly directional multi-beam steering, which is essential for the next generation of wireless communication. They also can improve the image quality in compressive imaging. Typically, the THz SLMs are volatile, where the switched state is lost when the external stimuli are removed thus persistent bias is required for each pixel. It raises difficulties in scaling up SLM because of the exponential increase in the number of control lines and the complexity of the feed network. To resolve this difficulty, we have to look for new solutions. The SLM with the memory function can preserve the transformed state in a non-volatile manner. Therefore, it can allow each pixel to be controlled serially, enabling us to simplify the control circuit and expand the number of pixels. Moreover, the SLM with memory function is highly expected for a reconfigurable holographic plate with high-fidelity. Therefore, the programmable metamaterial with memory is a promising alternative for THz SLM.

The metamaterials having memory behaviours in response to external stimuli have been realized using phase change materials (PCM). It relies on the hysteretic behaviors of PCM to external stimuli<sup>18-20</sup>. The memory metamaterials have exhibited many unusual electromagnetic behaviours such as dynamic resonance tuning<sup>19,20</sup>, reconfigurable logic-gate operation<sup>21,22</sup>, and greyscale data storage<sup>23,24</sup>. However, Programmable and pixelated memory metamaterials have not yet been realized. The main challenge for PCM based pixelated metamaterials is that the strong stimuli and thermal isolation are required for the independent control of each pixel, which induces unacceptable crosstalk between pixels.

Here we present a type of programmable memory metamaterials composed of 8×8 pixels at THz frequencies. To minimize the thermal crosstalk between adjacent pixels, we optimized our design to improve the thermal crosstalk. Each pixel is controlled under electrical excitation in a programmable manner, and the experimentally obtained modulation speed can reach ~1 kHz. This progress demonstrates its potential in applications requiring a high frame rate, such as THz beam scanning and compressive imaging. By exploiting the hysteresis effect of VO<sub>2</sub>, each pixel of the array can operate as a non-volatile memory. Each pixel could store multiple THz reflection amplitudes by applying a sequence of short current pulses with different peak amplitudes. Our work offers a general approach to develop programmable devices with memory behaviours.

### **Principles of programmable THz memory metamaterials**

As shown in Fig. 1, the programmable THz memory metamaterials consist of 8×8 pixels, each connected with an amplifier and an I/O port of field-programmable gate array (FPGA). Since the state of each pixel in the device could be switched independently, the programmable device could generate various THz spatial patterns such as 'N', 'J', and 'U'. The VO<sub>2</sub> patches are integrated into each pixel, and their hysteretic behaviours are utilized to realize the persistent storage of THz reflectance. Multiple states could be written and erased by applying current pulses with different amplitudes into a pixel. The designed device has the capability of multi-state THz image storage.

The optical picture of the proposed device and the microscopic image of a pixel is shown in Fig.2a,b. The pitch of each pixel is 1900 μm×1900 μm and ten rows and ten columns of unit cells are included in a pixel. The designed unit cell has a metal-insulator-metal (MIM) structure. For the top metallic layer, the VO<sub>2</sub> patches act as the active material in response to electrical stimuli. The gold bowtie antennas connected to the VO<sub>2</sub> patches are used to interact with the THz wave (see Supplementary Note 1 for details). The bottom metallic layer is continuous and acts as the ground plane. The 150-μm-thick *c*-cut sapphire substrate is sandwiched between two metallic layers.

The working principle of the designed device is similar to Salisbury screen<sup>25</sup>. The resonance frequencies mainly depend on the thickness and permittivity of the spacer. The VO<sub>2</sub>-metallic hybrid structures on the top metallic layer functions as the lossy screen. The THz reflection amplitude around the resonance frequency depends primarily on the conductance of VO<sub>2</sub> patches. We measured the THz reflection spectra at various temperatures in *x*-polarised normal incidence using THz time-domain spectroscopy (THz TDS).

As shown in Fig. 2d, the reflection amplitude around the resonance frequencies is sensitive to the change of the conductivity of VO<sub>2</sub>. As the conductivity of the VO<sub>2</sub> film increases, the reflection coefficient decreases, indicating it gradually approaches the perfect absorption condition. Meanwhile, the resonance frequency experiences a blueshift, mainly due to the rise of the coupling between the two antennas<sup>26</sup>. Besides, we altered the conductivities of VO<sub>2</sub> film and simulated the THz reflection spectra as shown in Fig. 2e. The simulation results validate our theoretical analysis and experimental results. Utilizing the VO<sub>2</sub> conductivity change during the phase transition, we realized the dynamic THz reflection with a modulation depth (*MD*) of more than 65%.

Thermal management is crucial for pixelated VO<sub>2</sub> devices. When external electrical stimuli trigger a pixel, lateral thermal diffusion can heat the surrounding pixels. To optimise the thermal conduction, we established a model in which the thermal conduction from a pixel to the surrounding pixels, substrate and stages are considered (see Supplementary Note 4 for the thermal model). We took the numerical calculation and found that the thermal conduction between the MIM structures and the stage is critical to suppress the thermal crosstalk. To achieve good thermal contact between the two objects, a layer composed of liquid metal, *i.e.* gallium-based alloy, with a thermal conductivity as high as 73 W/(m·K), was used to fill their gap.

To verify our thermal management design, we used a thermal infrared camera to measure the temperature distribution. To study the thermal crosstalk between pixels, we selected two pixels (labelled as P1 and P2), one pixel away as schematically shown in Fig. 3a. P1 and P2 were triggered by a voltage bias of 50 V and 30 V, respectively. Infrared thermal images of the device before and after applying voltage bias were captured. The temperature variation distribution was calculated based on the two images (see Supplementary Note 3 for the temperature calibration). As displayed in Fig. 3b, the temperature rise is remarkable in the regions of P1 and P2. A line scan along the blue dashed line in Fig. 3b is displayed at the bottom. The temperature increment at P1 and P2 was approximately 10 °C and 7 °C respectively. In contrast, the temperature increment at the pixel which bridges P1 and P2 was about 1 °C. It indicates that we suppressed the thermal crosstalk from the neighbouring pixels.

Meanwhile, we conducted the electrothermal simulation of the temperature distribution in the VO<sub>2</sub>- device using the finite element method (see Methods for details). We simulated the distribution of the temperature variation with the same voltage bias as the experiment. As shown in Fig. 3c, the simulation results indicate good agreement with the experimental results. In the corresponding line scan, there are sharp oscillations in the regions of P1 and P2. The fluctuation reflects the temperature contrast between the VO<sub>2</sub> patch and the surrounding bare substrate, as illustrated in the close-up view of P1 at the top of Fig. 3c. On the contrary, the oscillation was not observed in Fig. 3b because of the limited resolution of the thermal camera. In both experimental and simulated results, there is an evident temperature rise in the bias lines of P1 and P2. Since the resistance of the bias lines is non-negligible compared with the resistance of VO<sub>2</sub> patches in the metallic state, the ohmic loss results in a remarkable increase in temperature.

## Spatial THz modulation

The bias voltage could trigger the phase change of VO<sub>2</sub> and result in a remarkable change of conductivity. Correspondingly, the reflectance of the pixel experiences a noteworthy change. Therefore, the device can work as an electrically reconfigurable THz SLM. For SLM, the *MD* is defined as  $MD = |R_{i,on} - R_{i,off}| / R_{i,off}$  where  $R_{i,on}$  and  $R_{i,off}$  denote the reflection amplitude of the  $i^{\text{th}}$  pixel in 'on' and 'off' states, respectively. To verify its function as SLM, we generated THz patterns of 'N', 'J', and 'U' by switching on a combination of pixels optionally. We applied a voltage bias of 26 V to switch on a pixel. The collimated THz beam was used to shine the device, and the spatial distribution of the reflected THz beam was measured (see Supplementary Note 7 for experimental setup). A spatial map of *MD* could be obtained by measuring the spatial distribution before and after switching on the required pixels.

Figure 4a shows the spatial map of *MD* at 0.479 THz when the pattern of 'N' was generated by the device. The letter of 'N' is evident in the obtained map despite the variance of *MD* in the range of 23–65%. We also generated other patterns such as 'J' and 'U', and the obtained spatial maps of *MD* are displayed in Fig. 1. Meanwhile, we measured the temperature change when the pattern of 'N' was generated using a thermal camera (assuming an emissivity of 1). As shown in Fig. 4b, the letter of 'N' is also obtained since there is a remarkable temperature rise in the triggered pixels. In Fig. 4b, there is a bright vertical line in the middle, where the ground electrode is positioned. Since a large amount of current flow through the ground electrode, the non-negligible ohmic loss generates excess heat. The diffusion of the heat brings in thermal crosstalk to the neighbouring pixels. That is why we could see a bright spot at the bottom of Fig. 4a.

We found that the current bias is more suitable as the control signal of this device compared with the voltage bias. During the phase change process, there are several orders of magnitude drop in the resistance of VO<sub>2</sub> patches. If we used voltage bias as the control signal, the power would increase dramatically during the phase change process, making the thermal management challenging to implement. On the contrary, if we choose the current bias, the driving power drops continuously until the sample reaches thermal equilibrium. In the following, we adopt the current bias as the control signal.

We applied a square wave current with a peak amplitude of 60 mA to a pixel and measured the modulated reflection signal. Figure 4c shows the modulation amplitude of a pixel ( $\Delta R_i$ ) (the measured signal difference between 'on' and 'off' states for the  $i^{\text{th}}$  pixel) as a function of frequency. The 3 dB cut-off frequency was more than 1 kHz. That is much higher than previous reports<sup>20</sup>. As shown in Fig. 4d, when the modulation frequency increases to 1195 Hz, the THz reflection signal is periodically modulated with the same frequency. The increase of modulation speed is mainly attributed to the highly thermally conductive layer, which improves the thermal contact between the sample and the stage.

## Multi-state THz image storage

In Fig. 5a, the resistance–temperature curves of a pixel during the heating and cooling processes are shown. The phase transition process of VO<sub>2</sub> film is hysteretic, making the sample capable of retaining a ‘memory’ of the transformed state. When the external stimuli are removed, the resistance of VO<sub>2</sub> patches will stay at another steady state rather than returning to the initial state. Our device can, therefore, be treated as a memory array. In the following, we verify the multi-state memory operation of the device in response to current pulses with different amplitudes and pulse widths.

The current signal applied to one pixel for memory operation is shown in Fig. 5b. The stage temperature ( $T_{stage}$ ) was set to 50 °C, far below the  $T_c$ . A bias current of 40 mA was applied to achieve the maximum hysteresis. This bias is referred to as a ‘read’ signal. A current pulse signal with an amplitude higher than 40 mA is referred to as a ‘write’ signal. The pulse width was 10 s. Four different types of ‘write’ signals, with currents of 50 mA, 60 mA, 70 mA, and 80 mA, were applied. Besides, a 20-s-wide pulse with zero current was used as an ‘erase’ signal. When the ‘erase’ signal was applied, the pixel cooled down to  $T_{stage}$  and returned to its original state. We obtain the reflection amplitude of a pixel with a sequence of ‘read’, ‘write’ and ‘erase’ signal and then repeat the cycles with different ‘write’ signals. The corresponding normalised reflection amplitude as a function of time is shown in Fig. 5c. After applying four kinds of ‘write’ signals, the THz reflection amplitude would stay at the levels of 0.59, 0.55, 0.53, and 0.51 correspondingly during the “reading” process. The above results indicate that the THz reflectance of each pixel is non-volatile after application of a current pulse, *i.e.*, the *MD* of each pixel is stored in the memory

To verify multi-state storage capability in a programmable manner, we applied a ‘write’ signal of a 100-ms-wide current pulse to every pixel in a serial way. In this step, the  $T_{stage}$  was held close to the  $T_c$  of 56 °C to maximise the hysteresis effect. The letter ‘N’ was written into the 8×8 array by injecting different “write” current pulses into specific pixels. The 100-ms-wide current pulses with amplitudes of 20 mA, 30 mA, 40 mA, and 60 mA (Fig. 6a) were used to write the letter ‘N’. Maps of the *MD* at 0.429 THz obtained by raster scanning is shown in Fig. 6b. In all four pictures, the letter ‘N’ is clear, but there are remarkable differences in the brightness, which corresponds to the *MD*. We averaged the *MD* in the black box areas of the four spatial maps. Four different values in *MD* were obtained. As shown in Fig. 6c, the *MD* increase monotonously as the current increases

Utilising the four-state memory of the programmable device, we could spatially modulate the THz beam with greyscale. In the following, we selected four groups of pixels, and each group consisted of two pixels to form a loading-icon-like greyscale map as schematically illustrated in Fig. 6d. We injected the above four types of pulses into the four groups of pixels, respectively. A loading-icon-like greyscale image with four different greyscales was obtained, as shown in Fig. 6e. The various greyscales correspond to different *MD*. To measure the retention time of the state storage, we remeasured the spatial map of the *MD*, after 5 hours, as shown in Fig. 6f. We did not observe any apparent change in this figure, suggesting that the multi-state can be well stored for at least several hours.

## Conclusions

We have demonstrated an electrically programmable THz device with memory effects. Each pixel in the 8×8 array functions as an independent THz reflective modulator. The modulation speed greater than 1 kHz has been achieved after suppressing thermal crosstalk. The persistent spatial modulation of the THz wave with greyscales has been demonstrated, and the hold time was more than 5 hours.

In traditional SLM, each pixel is controlled by an individual bias line, which brings a technical challenge in integrating large-scale arrays. In our proposed devices, each pixel is non-volatile so that each pixel could be controlled serially. The memory effect liberates the SLM from persistent bias and offers the feasibility to adapt to the crossbar architecture<sup>27,30</sup>. The number of control lines, which equals the number of rows and columns for crossbar structures, could be reduced dramatically. Correspondingly, the feed network could be significantly simplified. Therefore, our work offers a pathway for the integration of large-scale SLM. Besides that, the working mechanism of memory devices is similar to the synapses of the human brain<sup>31,32</sup>. The memory SLM has the potential to simulate the human brain for calculation purposes<sup>33-35</sup>.

Furthermore, the hysterical effect has been found in a multitude of materials, such as PCM, two-dimensional materials<sup>22,27</sup>, perovskite<sup>28,29</sup>. By integrating these materials into the metadevices, the SLM capable of multi-state storage is extendable to a broad frequency range from microwave to visible light. The memory capability has the potential to serve as a core function for all future SLM.

## Methods

### Device fabrication

First, a layer of 200-nm-thick VO<sub>2</sub> film was deposited on a 150-μm-thick *c*-cut sapphire substrate by reactive magnetron sputtering<sup>36,37</sup>. Conventional photolithography was used to define the pattern. The VO<sub>2</sub> patches were structured via reactive ion etching in a CF<sub>4</sub> atmosphere with a flow rate of 40 sccm (standard-state cubic centimetre per minute) and an RF power of 100 W. Next, metallic films (10 nm-thick Ti and 200 nm-thick Au) were deposited on the bottom surface of the substrate via magnetron sputtering. After the second photolithography and metallic film (10 nm-thick Ti and 200 nm-thick Au) deposition, an array of bowtie antennas was formed on the top using the lift-off process. After the fabrication process, the sample was attached to the stage with a liquid metal layer as the thermally conductive adhesive.

### THz time-domain spectroscopy measurement

The THz TDS was used to measure the THz reflection spectra of the device at various temperatures. A fibre-based femtosecond laser was used to generate optical pulses centred at a 1560-nm wavelength with a repetition rate of 100 MHz. The output laser beam was split into two branches by a fibre splitter. The optical pulses in the two parts were guided to two fibre-coupled photoconductive antennas, which functioned as THz emitter and receiver, respectively. The THz wave from the THz emitter was collimated and focused on the device. The device was mounted on a heating stage, whose temperature was

adjusted by a temperature controller. The THz pulse reflected by the device was collected by the THz receiver. By scanning the optical delay line, the time-domain signals were sampled. After Fourier transform of time-domain signals and normalization with the reference signal, the reflection spectra were obtained.

## Electrothermal simulation of the temperature distribution

Besides the thermal crosstalk among the neighbouring pixels, the thermal diffusion from the device to the substrate, air and stage was also taken in account in the electrothermal model. The finite element method was used for numerical simulation. For the thermal boundary condition, the temperature of the conductive adhesive at the bottom was set to the  $T_{stage}$ . For the other surfaces exposed air, the boundary conditions were  $\mathbf{n} \cdot (\kappa \nabla T) = h (T - T_{air})$ , where  $\mathbf{n}$  is the outward-pointing unit vector normal to the surfaces,  $\kappa$  is the thermal conductivity,  $h$  is the heat transfer coefficient, and  $T_{air}$  is the ambient temperature. In the simulation,  $h = 20 \text{ W}/(\text{m}^2 \cdot \text{K})$  and  $T_{air} = 25 \text{ }^\circ\text{C}$ . Since the thermal crosstalk is the most serious when the  $\text{VO}_2$  patches go into the metallic state completely, we mainly calculated the thermal distribution when the sample temperature exceeds  $T_c$ . In that case, the thermal conductivity of  $\text{VO}_2$  was  $6.8 \text{ W}/(\text{m} \cdot \text{K})$ <sup>38</sup>, and the measured electric conductivity is  $1.5 \times 10^5 \text{ S}/\text{m}$ . The specific heat capacity and mass density were  $690 \text{ J}/(\text{kg} \cdot \text{K})$  and  $4340 \text{ kg}/\text{m}^3$ <sup>39</sup>. The thermal conductivity of the intermediate layer, a gallium-based alloy (Thermal Grizzly), was  $73 \text{ W}/(\text{m} \cdot \text{K})$ . Taking the gold film quality and the contact resistance between gold electrodes and  $\text{VO}_2$  patches into consideration, we chose 40% of the bulk conductivity ( $1.83 \times 10^7 \text{ S}/\text{m}$ ) as the conductivity of gold film for calculation<sup>40</sup>. Other properties of materials used in the simulation are listed in Table 1.

**Table 1:** Material properties used for heat capacity (C), density ( $\rho$ ) and thermal conductivity ( $\kappa$ ) in the numerical simulation.

$C_{\text{Al}_2\text{O}_3}$	$\rho_{\text{Al}_2\text{O}_3}$	$\kappa_{\text{Al}_2\text{O}_3}$	$C_{\text{Au}}$	$\rho_{\text{Au}}$	$\kappa_{\text{Au}}$
900 J/(kg·K)	3900 kg/m <sup>3</sup>	27 W/(m·K)	130 J/(kg·K)	19320 kg/m <sup>3</sup>	314 W/(m·K)

## Declarations

### Acknowledgement

This study was supported by the National Key Research and Development Program of China (2017YFA0700202), National Nature Science Foundation of China (61521001, 61731010, 62071217, 62027807, 61871212 and 61831012), Jiangsu Provincial Natural Science Fund (BK20170649), Fundamental Research Funds for the Central Universities, and Research Fund for Jiangsu Key Laboratory of Advanced Techniques for Manipulating Electromagnetic Waves. We acknowledge Hongbin Pan, Ting Xu, Feng Miao, Shijun Liang, Minghui Lu, Yijun Feng and Kebin Fan for fruitful discussions.

## Author contributions

Jingbo Wu, Benwen Chen and Biaobing Jin conceived the idea. Benwen Chen and Jingbo Wu designed the device. Qiang Xue, Yaojia Chi and Qiye Wen grew the VO<sub>2</sub> film. Benwen Chen fabricated the device. Benwen Chen and Weili Li built the terahertz setup and performed the terahertz experiment. Benwen Chen, Jingbo Wu, Biaobing Jin, Caihong Zhang, Jian Chen, and Peiheng Wu analyzed the experimental data. Biaobing Jin and Jingbo Wu instructed this work. Benwen Chen, Jingbo Wu and Biaobing Jin wrote the manuscript with contributions from all the authors.

## Data Availability

The data that supports the plots in this study and other findings of this study are available from the corresponding author upon request.

## References

1. Headland, D., Monnai, Y., Abbott, D., Fumeaux, C. & Withayachumnankul, W. Tutorial: Terahertz beamforming, from concepts to realizations. *APL Photonics* **3**, 051101 (2018).
2. Watts, C.M. et al. Terahertz compressive imaging with metamaterial spatial light modulators. *Nature Photonics* **8**, 605-609 (2014).
3. Xie, Z. et al. Spatial Terahertz Modulator. *Scientific Reports* **3** (2013).
4. Smith, D.R., Padilla, W.J., Vier, D.C., Nemat-Nasser, S.C. & Schultz, S. Composite medium with simultaneously negative permeability and permittivity. *Physical Review Letters* **84**, 4184 (2000).
5. Pendry, J.B. Negative Refraction Makes a Perfect Lens. *Physical Review Letters* **85**, 3966-3969 (2000).
6. Pendry, J.B., Schurig, D. & Smith, D.R. Controlling electromagnetic fields. *Science* **312**, 1780 (2006).
7. Cui, T.J., Qi, M.Q., Wan, X., Zhao, J. & Cheng, Q. Coding metamaterials, digital metamaterials and programmable metamaterials. *Light: Science & Applications* **3**, e218 (2014).
8. Gao, L.-H. et al. Broadband diffusion of terahertz waves by multi-bit coding metasurfaces. *Light: Science & Applications* **4** (2015).
9. Chan, W.L. et al. A spatial light modulator for terahertz beams. *Applied Physics Letters* **94**, 26 (2009).
10. Rout, S. & Sonkusale, S.R. A low-voltage high-speed terahertz spatial light modulator using active metamaterial. *APL Photonics* **1** (2016).
11. Savo, S., Shrekenhamer, D. & Padilla, W.J. Liquid Crystal Metamaterial Absorber Spatial Light Modulator for THz Applications. *Advanced Optical Materials* **2**, 275-279 (2014).
12. Kakenov, N. et al. Graphene-enabled electrically controlled terahertz spatial light modulators. *Optics Letters* **40**, 1984-1987 (2015).
13. Ferdous Hoque, M.N., Karaoglan-Bebek, G., Holtz, M., Bernussi, A.A. & Fan, Z. High performance spatial light modulators for terahertz applications. *Optics Communications* **350**, 309-314 (2015).

14. Dudley, D., Duncan, W. & Slaughter, J. Emerging digital micromirror device (DMD) applications, Vol. 4985. (SPIE, 2003).
15. Kappa, J. et al. Electrically Reconfigurable Micromirror Array for Direct Spatial Light Modulation of Terahertz Waves over a Bandwidth Wider Than 1 THz. *Sci Rep* **9**, 2597 (2019).
16. Kappa, J., Schmitt, K.M. & Rahm, M. Electromagnetic behavior of spatial terahertz wave modulators based on reconfigurable micromirror gratings in Littrow configuration. *Opt Express* **25**, 20850-20859 (2017).
17. Fšldesy, P., Fekete, Z., Párđy, T. & Gergelyi, D. Terahertz Spatial Light Modulator with Digital Microfluidic Array. *Procedia Engineering* **47**, 965-968 (2012).
18. Driscoll, T. et al. Memory Metamaterials. *Science* **325**, 1518-1521 (2009).
19. Liu, L., Kang, L., Mayer, T.S. & Werner, D.H. Hybrid metamaterials for electrically triggered multifunctional control. *Nat Commun* **7**, 13236 (2016).
20. Cai, H. et al. Multifunctional Hybrid Metasurfaces for Dynamic Tuning of Terahertz Waves. *Advanced Optical Materials* **6**, 1800257 (2018).
21. Manjappa, M. et al. Reconfigurable MEMS Fano metasurfaces with multiple-input-output states for logic operations at terahertz frequencies. *Nat Commun* **9**, 4056 (2018).
22. Migliato Marega, G. et al. Logic-in-memory based on an atomically thin semiconductor. *Nature* **587**, 72-77 (2020).
23. Carrillo, S.G.C. et al. A Nonvolatile Phase-Change Metamaterial Color Display. *Advanced Optical Materials* **7** (2019).
24. Pitchappa, P. et al. Chalcogenide Phase Change Material for Active Terahertz Photonics. *Advanced Materials* **31** (2019).
25. Salisbury, W.W. (Navy US., United States; 1952).
26. Zhang, B., Zhang, J., Zhang, B., Liu, C. & Wu, Z. in 2015 IEEE 4th Asia-Pacific Conference on Antennas and Propagation (APCAP) 146-147 (2015).
27. Lee, H.-S. et al. Dual-Gated MoS<sub>2</sub> Memtransistor Crossbar Array. **30**, 2003683 (2020).
28. Kang, K. et al. High-Performance Solution-Processed Organo-Metal Halide Perovskite Unipolar Resistive Memory Devices in a Cross-Bar Array Structure. *Adv Mater* **31**, e1804841 (2019).
29. Kim, H. et al. Quasi-2D halide perovskites for resistive switching devices with ON/OFF ratios above 109. *NPG Asia Materials* **12** (2020).
30. Fuller, E.J. et al. Parallel programming of an ionic floating-gate memory array for scalable neuromorphic computing. **364**, 570-574 (2019).
31. Kuzum, D., Yu, S. & Wong, H.S. Synaptic electronics: materials, devices and applications. *Nanotechnology* **24**, 382001 (2013).
32. van de Burgt, Y. et al. A non-volatile organic electrochemical device as a low-voltage artificial synapse for neuromorphic computing. *Nat Mater* **16**, 414-418 (2017).

33. Weng, J. et al. Meta-neural-network for real-time and passive deep-learning-based object recognition. *Nat Commun* **11**, 6309 (2020).
34. Yao, P. et al. Fully hardware-implemented memristor convolutional neural network. *Nature* **577**, 641-646 (2020).
35. Wang, Z. et al. Fully memristive neural networks for pattern classification with unsupervised learning. *Nature Electronics* **1**, 137-145 (2018).
36. Wen, Q.-Y. et al. Terahertz metamaterials with VO<sub>2</sub> cut-wires for thermal tunability. *Applied Physics Letters* **97**, 021111 (2010).
37. Xiong, Y. et al. Tuning the phase transitions of VO<sub>2</sub> thin films on silicon substrates using ultrathin Al<sub>2</sub>O<sub>3</sub> as buffer layers. *Journal of Physics D: Applied Physics* **47** (2014).
38. Jr., W.J.K. & Proto, G.R. Properties of Vanadium Dioxide Thermal Filaments. **42**, 2140-2142 (1971).
39. Li, D. et al. Joule Heating-Induced Metal-Insulator Transition in Epitaxial VO<sub>2</sub>/TiO<sub>2</sub> Devices. *ACS Appl Mater Interfaces* **8**, 12908-12914 (2016).
40. Johnson, P.B. & Christy, R.W. Optical Constants of the Noble Metals. *Physical Review B* **6**, 4370-4379 (1972).

## Figures

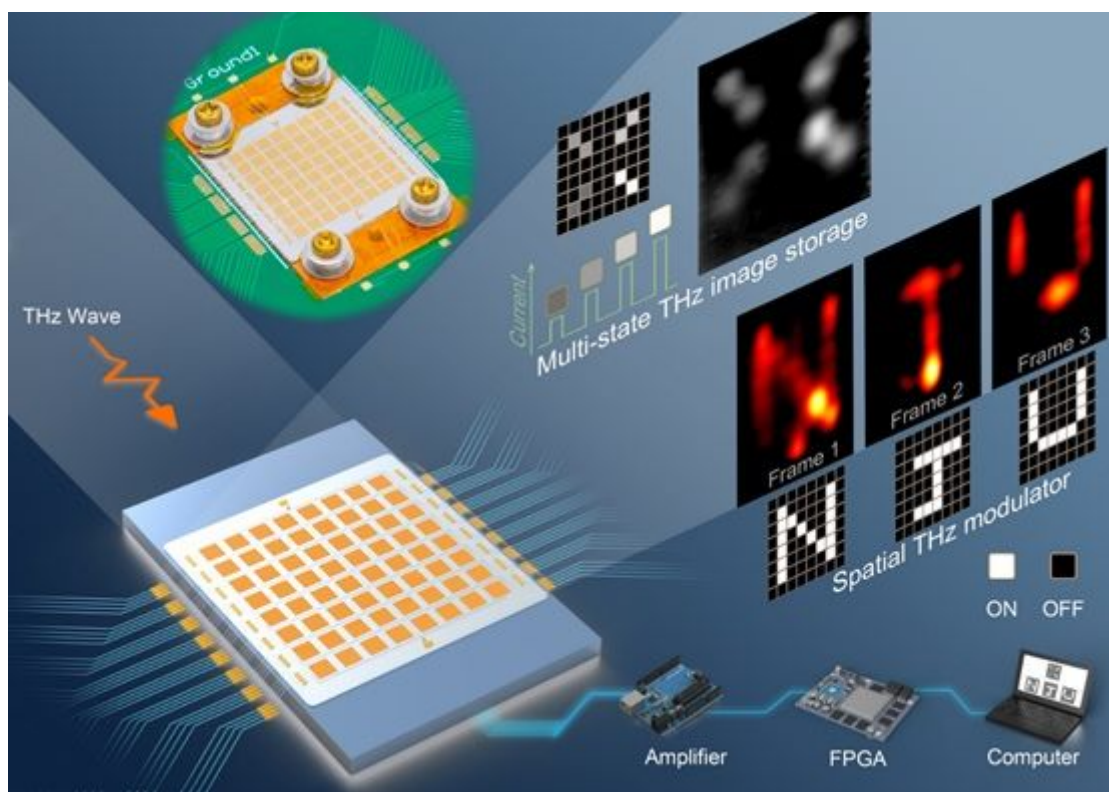
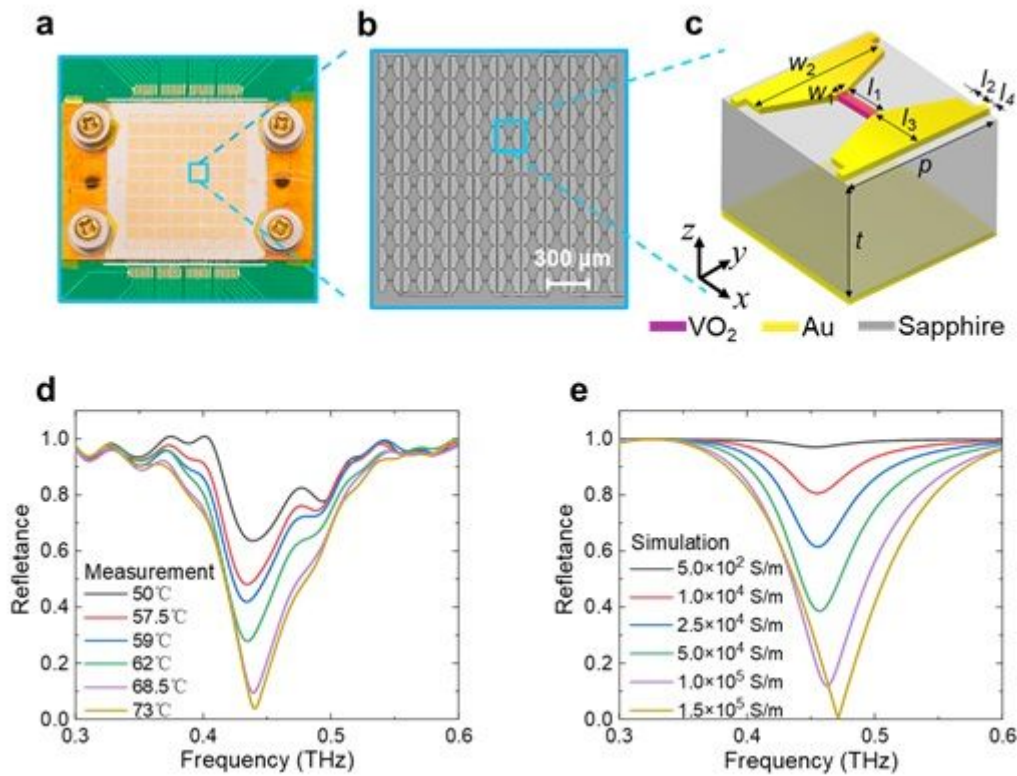


Figure 1

Schematic illustration and optical image of the proposed VO<sub>2</sub>-based THz memory metamaterials. The device consists of 8×8 pixels, and each pixel is controlled independently using FPGA and amplifier. The metamaterials have two functions: multi-state THz image storage and spatial THz modulator. The photo of the fabricated device is shown at the upper left.



**Figure 2**

Device structure and tuneable THz reflection spectra. (a) Top view of the fabricated device. (b) Microscopic image of a pixel composed of 10×10 unit cells. (c) Schematic diagram of a unit cell. Parameters for the unit cell:  $p = 160 \mu\text{m}$ ,  $l_1 = 40 \mu\text{m}$ ,  $w_1 = 10 \mu\text{m}$ ,  $l_2 = 32 \mu\text{m}$ ,  $w_2 = 140 \mu\text{m}$ ,  $l_3 = 52 \mu\text{m}$ ,  $l_4 = 10 \mu\text{m}$ ,  $t = 150 \mu\text{m}$ . (d) Measured THz reflection spectra at different temperatures without electrical bias. (e) Simulated reflection spectra as different conductivity of VO<sub>2</sub>.

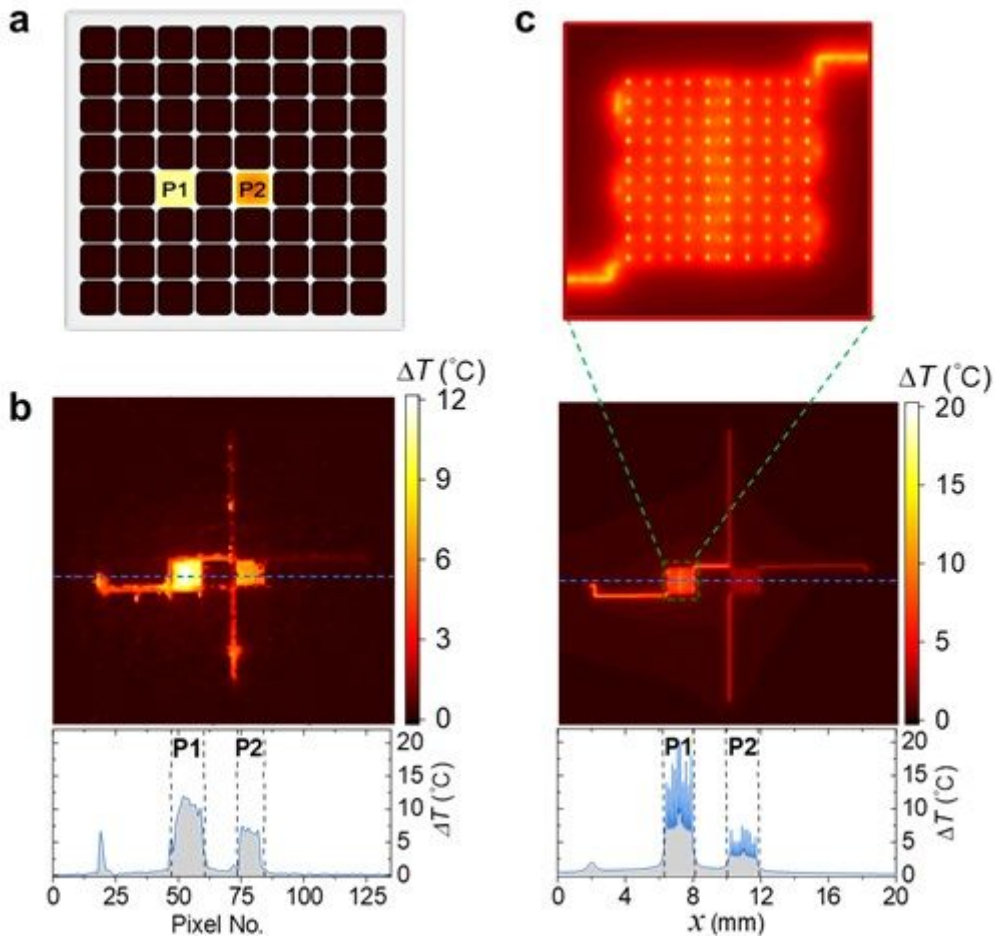


**Figure 3**

Spatial temperature distribution of the pixelated device. (a) Schematic of the 8x8 array with two triggered pixels. The two pixels which are a pixel away are named P1 and P2. P1 and P2 were triggered by voltage biases of 50 V and 30 V, respectively. (b) Measured distribution of temperature difference before and after the external voltage bias is applied ( $T_{\text{stage}}=55\text{ }^{\circ}\text{C}$ ) using a thermal camera. The line scan of the temperature difference across the blue dashed line is shown at the bottom. (c) Simulation distribution of temperature difference based on the finite element method. The figure at the top is the close-up view of the P1 region. The image at the bottom is the line scan of simulated temperature difference along the blue dashed line.

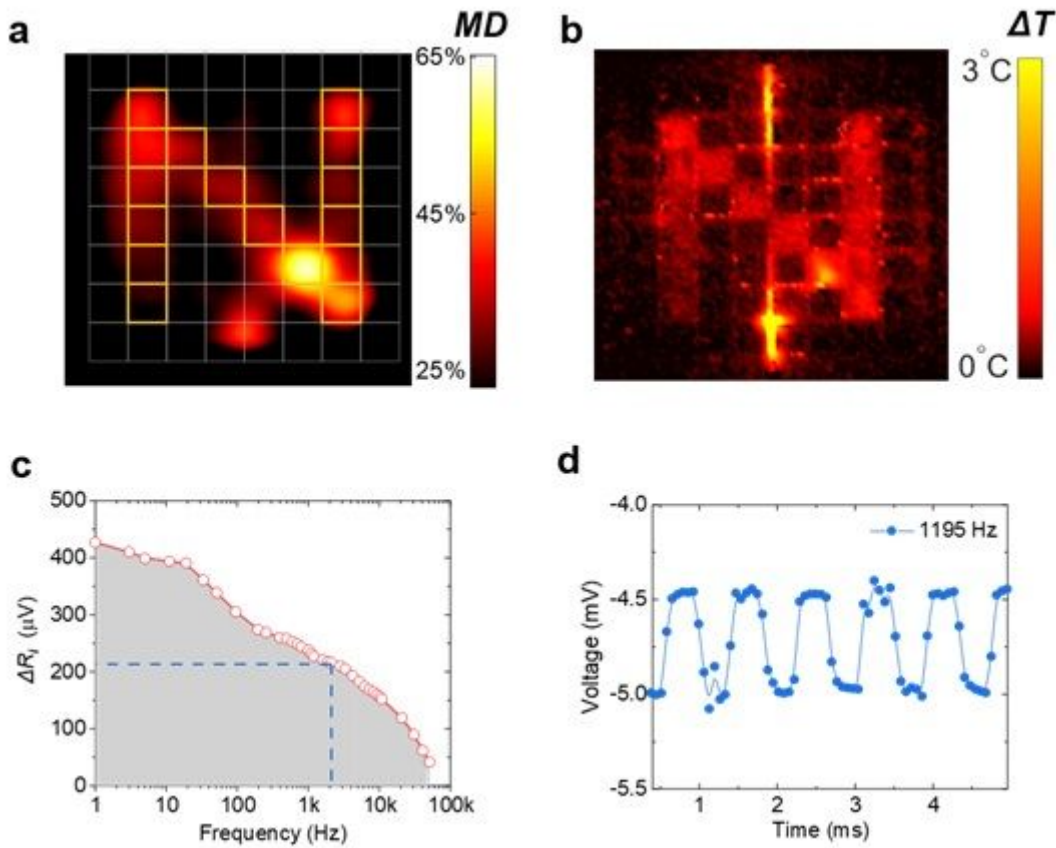


**Figure 4**

Spatial modulation of reflected THz wave. (a) Measured spatial map of the MD at 0.479 THz ( $T_{\text{stage}} = 52\text{ }^{\circ}\text{C}$ ). The pixels marked with a yellow line outline were applied with a bias voltage of 26 V, while the others were not biased. The outline of  $8 \times 8$  pixels in the array is marked with grey lines. (b) Measured temperature difference before and after the bias is applied using a thermal camera. (c) Measured  $\Delta R_i$  as a function of the modulation frequency. (d) Modulated time-domain signals at a frequency of 1195 Hz.

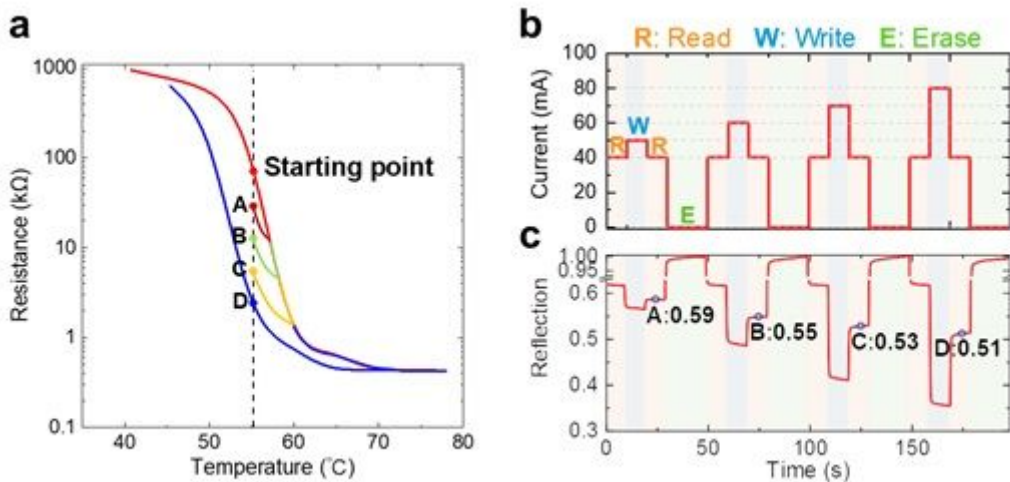


**Figure 5**

Memory effect in the VO<sub>2</sub> device. (a) The measured resistance-temperature characteristic of a pixel. Four hysteresis loops correspond to the four states (labelled with A, B, C and D respectively). (b) A sequence of ‘read’, ‘write’, and ‘erase’ current signals used for the multi-state THz memory operation. (c) Time-domain signal of the reflected THz wave at 0.429 THz when the current signal shown in Fig. 5b was applied to a pixel. The reflection amplitude is normalized by the amplitude in the initial state.

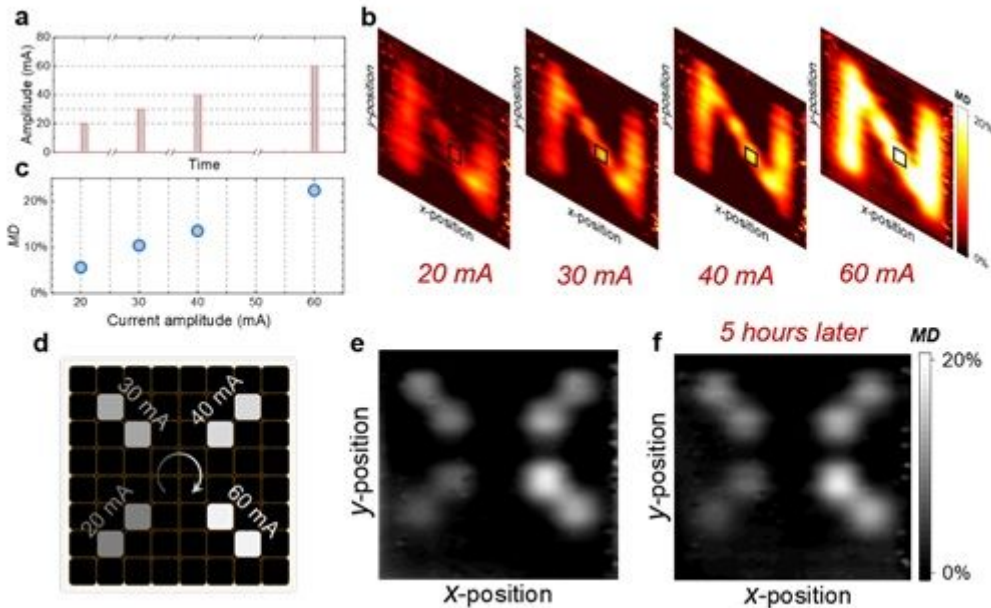


**Figure 6**

THz multi-level memory devices. (a) A sequence of current pulses with amplitudes of 20 mA, 30 mA, 40 mA, and 60 mA used to write the letter ‘N’. (b) Measured spatial maps of MD at 0.429 THz ( $T_{\text{stage}} = 56\text{ }^{\circ}\text{C}$ ) with four different current pulses shown in Fig. 6a as ‘write’ signals. The letter of ‘N’ is evident in all four images but varies in MD. (c) Average value of MD in the black box area of Fig. 6b as a function of the peak current. (d) Loading-icon-like schematic formed by four groups of pixels. Current pulses trigger pixels in different groups with different amplitudes. (e) Measured loading-icon-like grey image. Four different grey scales corresponding to different MD. (f) Spatial map of the MD measured at 5 hours later.

## Supplementary Files

This is a list of supplementary files associated with this preprint. Click to download.

- [SIProgrammableterahertzmetamaterialswithnonvolatilememory2021.02.28.docx](#)
- [Supplementaryvideo.wmv](#)